

AN ADJOINT BASED GRADIENT OPTIMIZATION CHAIN FOR COMPLEX HELICOPTER FUSELAGE PARTS USING A FREE FORM DEFORMATION OR CAD BASED PARAMETERIZATION METHOD

Marc Wentrup*

* Institute for Aerodynamics and Flow Technology, DLR

Abstract

In this paper a gradient based optimization chain for aerodynamic shape optimization is described. The chain includes the DLR TAU-code for flow evaluations, while a discrete adjoint approach is used to compute the gradient of a high count of design variables. For parameterization of complex helicopter fuselage parts, two different methods were implemented. The first method uses the Free Form Deformation technique to modify the shape by manipulating the control points of a NURBS-volume. The second approach is to use the CAD software CATIA V5 to build up a parametrical model for optimization. To investigate both methods with different settings, the ROBIN-mod7 fuselage was chosen to reduce drag by optimizing the relative simple back door geometry. After gaining experience with this example, the optimization chain is used to optimize the shape of the common helicopter platform sponsons in the scope of the European Clean Sky GRC2-project. It could be shown that for both examples a reduction of the drag force was achieved (drag reduction of 21.76% for the ROBIN-mod7 test case and 1.49% drag reduction for the sponsons optimization).

NOMENCLATURE

\bar{A}	deformation Matrix
C_d	drag coefficient
D	design variables
H/C	helicopter
I	cost function
L	Lagrangin function
N	B-spline basis function
\vec{P}_l	point coordinats in a NURBS volume
\vec{Q}	control points of a NURBS volume
R	residual
\vec{R}	modified control points of a NURBS volume
V_∞	flow velocity [m/s]
W	flow variables
i,j,k	indices
x,y,z	coordinates [m]
Λ	Lagrangin multiplier
α	fuselage angle of attack [deg]
α_i, β_i	coefficients of volume spline

1. INTRODUCTION:

The design of modern helicopter fuselage is not only driven by its utility aspects but also by its aerodynamic properties. The demand for higher cruise speed and lower fuel consumptions requires in general a reduction of the parasite drag that is caused by the fuselage and its attached parts. This could be done by locally optimizing the shape of specific parts. To consider a large range of possible designs, it is useful to evaluate a high number of design variables during the optimization task. Additionally the flow has to be solved by a high fidelity CFD-code to sufficiently resolve the complex flow conditions and interference effects of a helicopter fuselage. For an efficient optimization, an algorithm should be chosen that needs a minimum number of flow evaluations, depending on the design variables count. For these purposes, a gradient based optimization seems to be most promising. By using an adjoint approach it is possible to decouple the gradient computation from the flow variables [1][2]: only one flow evaluation and solving the adjoint equation is needed to get the gradient, independent from the number of design variables. With the TAU-code, the DLR possesses a tool that is able to solve the RANS and the adjoint equation [2][3]. To use this code for shape optimization, it has to be coupled with an appropriate method to parameterize the target surface. The Free Form Deformation technique (FFD) shows to have a good shape control with relatively few design variables [4]. This technique is also available as option for grid deformation in the TAU-code and

provides an easy handling of the parameterization as only a structured box, surrounding the target surface, has to be defined. This technique had already been used for several investigations in the past [5][6][7].

Nevertheless, in some cases it is not only required to find an optimum shape deformation but also to find an optimum positioning or scale of a given structure like a stabilizer or a fillet for example. For these task it would be beneficial, to use a CAD-based parameterization. CATIA V5 [8] is a common CAD software that has the functionality of generating the required parametrical surface model. Additionally, it provides several functions to generate surfaces that can be deformed similar compared to FFD parameterization. The drawback of this solution is that a lot of experience is needed to create a stable model that returns a valid CAD-output for a wide range of possible parameter variations.

Because of the different advantages, both methods were coupled with the TAU-code to form an automatic optimization chain.

The properties of this optimization tool are tested on a blunt fuselage optimization task, using the ROBIN mod7 fuselage [9]. Additionally the chain is used in the scope of the Clean Sky GRC-2 project to optimize the sponsons shape of the GRC-2 common H/C platform [10].

2. THE OPTIMIZATION CHAIN

The optimization chain uses the CFD-solver TAU to compute the steady RANS equation and the integrated adjoint solver to evaluate the adjoint equation. The shape parameterization and deformation is done either by a Free Form Deformation technique (FFD) or by using CATIA V5 (CAD-based). To adapt the computational grid to the new shape, a Radial Base Function method is used for grid deformation (RBF-deformation).

The schematic structure of the optimization chain is shown in Figure 1. It is build up in a python environment, consisting two major classes. The first class (Figure 1 green) manages the shape deformation tasks. It takes the design variables values as input and activates the parameterization method (FFD or CAD-based) to get the displacement vectors of the start surface to the deformed surface. These vectors could be used to directly deform the computational grid by RBF-deformation or it will return these vectors in cases, where the grid deformation is not executed on the local work station (for gradient computation for example).

The second class is responsible for the communication between the local work station and

the high performance computer cluster (Figure 1 orange). Depending if either the actual value of the cost function or the gradient is needed, it copies all required data to the cluster and starts the corresponding job to solve the flow or the adjoint equations (Figure 1 blue). After these jobs finished, the class gets the relevant data back to the local work station and returns them to the design process (Figure 1 yellow).

The optimization process here consists of a 1-D line search that captures the optimal step size with a 3-point pattern following the conjugate gradient as formulated by Fletcher and Reeves [9]. One design cycle consists of getting the cost function of the previous cycle, computation of the gradient and performing the 1-D line search (Figure 1 purple) till an optimum of this design cycle is found. These steps are repeated until a satisfying solution is found.

2.1. Flow solver

In this paper the cost function is evaluated by solving the compressible Reynolds-averaged Navier-Stokes equation with the DLR TAU-code [12]. Beside the ability of solving flow conditions, TAU possesses several additional modules like an adjoint solver and a deformation module for example.

For flow evaluations the code uses an edge-based dual-cell approach, which makes it suitable for hybrid computational meshes. For the optimization tasks, the steady state RANS-equations are solved with a central Jameson scheme for special discretization to express the inviscid fluxes with scalar dissipation. Time integration is done by an implicit backward Euler scheme, solved with LU-SGS. The convergence progress is accelerated, using a three level multigrid, while turbulence modelling is realized with the one-equation Spalart-Almaras model [13].

To additionally accelerate the flow evaluation during the optimization process the result of the previous design cycle is used as start solution. By using a Cauchy convergence criteria the evaluation is considered as sufficiently converged when the lift and drag coefficients have no changes higher than a $10e-5$ magnitude during the last 1000 iterations or if the residual drops lower then $10e-11$ magnitudes. In cases, where these criteria are not reached, a maximum of 25000 additional iterations for the ROBIN-mod-7 task (50000 for the Common H/C platform sponson) are computed. To ensure a reliable evaluation of the cost function value, the average value of the last 1000 iterations is considered for the optimization algorithm.

2.2. Discrete Adjoint Formulation

To avoid a re-computation of the flow solution for each perturbed design variable in order to calculate the cost functions gradient by finite differences, the discrete adjoint formulation can be applied. This formulation decouples the gradient computation from the flow variables with the consequence that only one flow evaluation is necessary to get the gradients. Additionally the adjoint equation has to be solved. This equation is derived from the general gradient formulation of a cost function $I = I(W(D), D)$:

$$(1) \quad \frac{dI}{dD} = \frac{\partial I}{\partial D} + \frac{\partial I}{\partial W} \frac{\partial W}{\partial D}$$

$W(D)$ is the vector of the flow variables, depending from the design variables D . Assuming that the flow residual R is very small, the so called Lagrangian function:

$$(2) \quad L = I + \Lambda^T R \approx I; \quad R \approx 0$$

can be used to replace the cost function I in the gradient formulation:

$$(3) \quad \frac{dL}{dD} = \left[\frac{\partial I}{\partial D} + \frac{\partial I}{\partial W} \frac{\partial W}{\partial D} \right] + \Lambda^T \left[\frac{\partial R}{\partial D} + \frac{\partial R}{\partial W} \frac{\partial W}{\partial D} \right]$$

where Λ is designated as Lagrangian multiplier. After collecting all terms with $\frac{\partial W}{\partial D}$ this expression can be written as:

$$(4) \quad \frac{dL}{dD} = \left[\frac{\partial I}{\partial W} + \Lambda^T \frac{\partial R}{\partial W} \right] \frac{\partial W}{\partial D} + \frac{\partial I}{\partial D} + \Lambda^T \frac{\partial R}{\partial D}$$

At this point it gets clear, that the dependence of the gradient from the flow variables W can be eliminated by setting the bracket term equal zero:

$$(5) \quad \left[\frac{\partial I}{\partial W} + \Lambda^T \frac{\partial R}{\partial W} \right] = 0$$

This leads directly to the so called adjoint equation:

$$(6) \quad -\frac{dI}{dW} = \Lambda^T \frac{\partial R}{\partial W}$$

To solve this equation a Krylov method (here GMRes) is combined with either an iterative multigrid preconditioner or with a defect correction preconditioner, using a SAMG [14] inner solver. After evaluating Λ the gradient computation is reduced to:

$$(7) \quad \frac{dI}{dD} \approx \frac{dL}{dD} = \frac{\partial I}{\partial D} + \Lambda^T \frac{\partial R}{\partial D}$$

where $\partial I/\partial D$ and $\partial R/\partial D$ can be cheaply approximate with finite differences by perturbing each design variable with ΔD :

$$(8) \quad \frac{dI}{dD} \approx \frac{\Delta I}{\Delta D} + \Lambda^T \frac{\Delta R}{\Delta D}$$

2.3. Shape parameterization

For automatic shape optimization it is necessary to relate the surface shape to a set of parameters. These parameters are used as design variables during the optimization process. In the following parts, two possible solutions for this problem will be presented.

2.3.1. Free Form Deformation

The Free Form Deformation technique provides an appropriate surface control with a relatively low count of design variables. This is done by mapping all points \vec{P}_l of the target surface from the Cartesian coordinate system into a B-spline volume with $\vec{Q}_{i,j,k}$ control points:

$$(9) \quad \vec{P}_l = \sum_{i=0}^{nu} \sum_{j=0}^{nv} \sum_{k=0}^{nw} N_{i,m_u}(u) N_{j,m_v}(v) N_{k,m_w}(w) \vec{Q}_{i,j,k}$$

The point location (u_l, v_l, w_l) for each surface point \vec{P}_l is evaluated by a Newton iteration method. By moving the control points from $\vec{Q}_{i,j,k}$ to $\vec{R}_{i,j,k}$, the re-mapping of the surface points to the Cartesian coordinates will return a modified location of each surface point. All steps of the FFD are summarized in Figure 2. For further information the reader is referred to [4].

This technique had been implemented in the deformation module of the TAU-code and can be used to deform the surface grid by defining a structured control box that wraps the target surface. To reduce the computational costs it is possible to use a surrogate grid that only contains the target surface for FFD and returns the deformation vectors of each grid node to adapt the computational mesh by RBF-deformation. This way it is also possible to define geometrical constraints by limiting the displacement vectors.

2.3.2. CAD based parameterization

With the CFD software CATIA V5 from Dassault Systèmes a parametrical surface model can be build up. With the design table functionality it is possible to use this model in an automatic shape deformation algorithm. Therefore the optimizer modifies the values in an external table file, which is read in by a CATIA macro that returns the deformed model as CAD output.

To adapt the computational mesh by RBF-deformation to the deformed surface, it is necessary to compute the displacement vectors of the shape changes. Therefore the CAD output is read in by a grid generation software. At this place, ANSYS-ICEMCFD is used to update a structured surface

mesh for the new shape. The deviation of the grid node between the initial and the updated grid provides the required deformation vectors.

2.4. Adaption of the computational mesh

To adapt the computational mesh to the new surface shape there are in general two possibilities. The first one is the regeneration of the mesh. The adjoint approach requires exactly the same grid topology between initial and the deformed mesh. This can be easily ensured by structured meshes. For complex shapes it is also difficult to ensure a robust automatic mesh generation. The second possibility consists of deforming the computational mesh to fit the modified surface. During this study, the displacement $(\Delta x, \Delta y, \Delta z)$ of the volume mesh nodes at (x, y, z) is interpolated with a radial base function from the displacement vector $(\Delta x_j, \Delta y_j, \Delta z_j)$ of the initial surface points (x_j, y_j, z_j) . By using a classic volume spline as radial base function, the displacement of each mesh node can be represented as:

(10)

$$\Delta x(x, y, z) = f(w_d)(\alpha_{1,x} + \alpha_{2,x}x + \alpha_{3,x}y + \alpha_{4,x}z) + \sum_i^N \beta_{i,x} \sqrt{(\Delta x_i)^2 + (\Delta y_i)^2 + (\Delta z_i)^2}$$

where α_i and β_i can be calculated by solving the following set of linear equations:

$$(11) \quad \Delta \underline{x} = \bar{\bar{A}} \begin{pmatrix} \alpha_x \\ \beta_x \end{pmatrix}, \Delta \underline{y} = \bar{\bar{A}} \begin{pmatrix} \alpha_y \\ \beta_y \end{pmatrix}, \Delta \underline{z} = \bar{\bar{A}} \begin{pmatrix} \alpha_z \\ \beta_z \end{pmatrix}$$

and $f(w_d)$ is a weight function, depending on the wall distance w_d . This function can be used to control the abate rate of the deformation in space.

The interpolation matrix $\bar{\bar{A}}$ is a $(N + 4) \times (N + 4)$ matrix, with N corresponding to the number of the given displacement vectors. As the displacements of each node are interpolated, it is not necessary that the base points of the displacement vectors fit the surface grid points. This way it is possible to reduce the costs of inverting the interpolation matrix by simply reducing the number of deformation vectors. Nevertheless it should be pay attention that the distribution of the displacement vectors over the target surface ensures an adequate deformation of the computational mesh surface.

3. ROBIN-MOD7

3.1. Configuration and flow conditions

The ROBIN-mod7 fuselage is a modified version of the original generic ROBIN fuselage [9]. The

modification consists of the replacement of the stream lined fish tail by a blunt afterbody section that corresponds to a typical fuselage shape of a helicopter with a back door for rear loading capabilities (see Figure 3). This model was established as baseline for active flow control investigations on blunt after bodies [9][15][16]. Due to these previous investigations, the flow around this fuselage is already well documented by CFD and wind tunnel results. Therefore, this configuration is chosen to validate the adjoint based gradient optimization chain. For these purpose, the baseline test case, described in [9], was chosen. The optimization task was defined to reduce total drag by shape modification of the rear part (see Figure 3 (blue surface)).

The flow conditions were chosen as described in [9]. Therefore the model was scaled to a length of 0.7172m which leads to a Reynolds number of approximately 1.67 million by applying a free stream velocity of 34 m/s (Mach \approx 0.1). Compared to the experiment in [9], the wind tunnel walls and the model support were neglected and the model was simulated in a spherical control volume with farfield boundary conditions and a fuselage pitch angle of $\alpha = 0^\circ$. The relevant data for the flow conditions are summarized in Table 1.

Table 1: Flow condition for ROBIN-mod-7 optimization

α [°]	V_∞ [m/s]	Ma [-]	ref. length [m]	ref. area [m ²]	Re [10 ⁶]
0	34	0.1	0.7172	0.015	1.67

3.2. Computational grid

To investigate the influence of the computational mesh on the optimization results, three grids with different resolutions were generated (see Figure 4). The mesh was generated with the grid generation software Pointwise [17]. For all cases, the fuselage model was situated in the middle of a sphere with a $10 \times l$ radius ($l = \text{model length} = 0.7172\text{m}$). The boundary layer is resolved by a 20 mm thick prism layer with 30 points. The coarsest grid has a total point number of 0.8 million, the medium resolved mesh contains 2.1 million points and the finest mesh has 3.9 million points.

3.3. Shape parametrization

3.3.1. Free Form Deformation

The Free Form Deformation technique was applied on a simplified surrogate grid with less surface points. This is done to reduce the dimension of the interpolation matrix $\bar{\bar{A}}$ for the RBF-deformation to save computational costs. The parameterization of the back door is investigated with two different shapes of FFD control boxes. The first approach is

to surround the target surface with an orthogonal box, where the design parameters are defined by displacing the control points along the orthogonal direction of the boxes surfaces. As consequence, the number of design variable per control point depends on the number of surfaces to which the point is adjoined (points on edges: 2 design variables; points on vertices: 3 design variables). To reduce the design variable count, the symmetry of the model was used. Additionally the front and the upper faces of the box were fixed, to avoid a strong deformation of the connecting line between target surface and the rest of the fuselage (see Figure 5 (left)). The applied box has the dimension $i=6$, $j=4$ and $k=4$. Regarding the described arrangement, this leads to a total number of 47 design variables.

The second approach is to form a control box that is adapted to the shape of the target surface. For this solution, the design variables are defined as control point displacement, orthogonal to the target surface. Analog to the first approach, the control points on the front and the upper edge of the box are fixed to avoid a deformation of the surface connection (see Figure 5 (right)). The applied box has the dimension $i=8$, $j=6$ and $k=2$. This leads to 30 design variable. Additionally a version with 56 design variables ($i=10$, $j=8$, $k=2$) was used to investigate the influence of the design variable count.

3.3.2. CAD based parameterization

Due to the symmetry, the half back door surface was re-modelled with CATIA V5 by using the loft function. Beside the intersection lines of the back door and the rest fuselage, 5 lateral cut profiles and one longitudinal cut profile (intersecting line with the

$y=0$ symmetry plane) were generated to define the loft (see Figure 6). The profiles consist of B-spline curves with 9 control points. The control points are defined as endpoints of five lines that had been arranged like spokes in a circular quadrant on each cut plane as illustrate in Figure 6. The intersection points of the surrounding structures with the cut plains are used as start/end points of the B-splines. To provide a smooth transition between the target surface and the fixed surfaces of the fuselage, an additional control point is situated 5 mm in tangential direction to the intersection curve of the cut planes and the surrounding surfaces (see Figure 6). By using the spoke lines length as design variables (30 design variables), the shape of the back door surface can be modified relatively free. A second version with 6 lateral profiles, defined by 9 spokes per cut plane provides 54 design variables.

3.4. Test Matrix

Beside the different parameterization types and the three different computational meshes, several additional parameters were investigated in this study. In Table 2 all considered test cases are listed. The medium resolved mesh was selected as standard grid for the parameter variation of the perturbation step size and the design variable count. These parameters were investigated for the CAD-based and the FFD parameterization, while the change of the adjoint solving method is only tested with the squared FFD control box in combination with the medium resolved grid, as this parameterization strategy provides the largest possible shape modulation.

Table 2: ROBIN-mod7 optimization test matrix

Name	Parameterization methode	design variables	Mesh	Adjoint preconditionor	ΔC_d
RB7_FFD_ad_30_m1	FFD with surface adapted control box	30	coarse mesh (m1)	Iterative multigrid	16.63%
RB7_FFD_ad_30_m2	FFD with surface adapted control box	30	Medium mesh (m2)	Iterative multigrid	18.2%
RB7_FFD_ad_30_m2_samg	FFD with surface adapted control box	30	Medium mesh (m2)	defect correction (samg)	18.1%
RB7_FFD_ad_56_m2	FFD with surface adapted control box	56	Medium mesh (m2)	Iterative multigrid	14.6%
RB7_FFD_ad_30_m3	FFD with surface adapted control box	30	fine mesh (m3)	Iterative multigrid	15.1%
RB7_FFD_sq_47_m2_1	FFD square control box	47	Medium mesh (m2)	Iterative multigrid	16.4%
RB7_FFD_sq_47_m2_1_samg	FFD square control box	47	Medium mesh (m2)	defect correction (samg)	19.95%
RB7_CAD_30_m1	CATIA V5 (CAD)	30	coarse mesh (m1)	Iterative multigrid	13.8%
RB7_CAD_30_m2	CATIA V5 (CAD)	30	medium mesh (m2)	Iterative multigrid	17.69%
RB7_CAD_54_m2	CATIA V5 (CAD)	54	Medium mesh (m2)	Iterative multigrid	19.53%
RB7_CAD_30_m2_samg	CATIA V5 (CAD)	30	medium mesh	defect	8.3%

			(m2)	correction (samg)	
RB7_CAD_30_m3	CATIA V5 (CAD)	30	fine mesh (m3)	Iterative multigrid	21.76%

3.5. Results

3.5.1. Baseline

The start reference for the optimization process returns a drag coefficient between 0.1219 (medium grid) and 0.1247 (coarse grid) which corresponds approximately to the values that had been investigated in [9] ($0.101 < C_d < 0.169$). Additionally, the deviation of the predicted coefficients of the medium and the fine grid shows to be small ($\Delta C_d \approx 0.0005$; $\Delta C_l \approx 0.0019$).

Figure 7 shows that the baseline flow is dominated by a large flow separation at the blunt rear fuselage. For all three meshes, the separation line is predicted similar and it can be observed that the flow is not symmetrical on the back door area.

Before starting the optimization process, a perturbation step size has to be chosen for the gradient computation. By choosing a too large step size, the utilisation of finite differences to solve $\partial I / \partial D$ and $\partial R / \partial D$ (see Chapter 2.2) will return a wrong gradient, while using a too small step size will increase the influence of noise effects of the adjoint solution on the gradient. Therefore the sensitivity of each design variable was computed with four different perturbation step sizes (10mm, 1mm, 0.1mm and 0.01mm). Due to the normalization of the grid deformation, the step size value describes the maximum surface deformation, caused by the design variable perturbation. It turns out, that the medium and the finest mesh return consistent gradients, while the coarse grids results deviate significantly for all parameterization types. In the considered range, no significant influence of the step size could be observed. The usage of different preconditioning approaches for the adjoint solution returns a higher influence due to the better convergence of the defect correction method.

3.5.2. Free Form Deformation

For each test case in Table 2 the optimization was performed with 10 design cycles. Depending on the 1-D line search a total number of up to 100 flow solutions were evaluated. Figure 8 show the history of the drag reduction during the optimizations with the FFD parameterization, using a surface adapted deformation box. Independent from the computational grid and the number of design variables, a maximum drag reduction between approximately 14% and 18% was found. The highest drag reduction was found with 18.2% for the test case with 30 design variables and the medium resolved mesh. In cases where the grid deformation

causes a destruction of the computational grid, a high penalty value for the cost function was returned to avoid the optimizer to proceed further in this direction. Such cases can be mainly observed for the optimization with the coarse grid and occasionally for the case with the finest mesh.

Figure 9 shows the drag reduction history for the FFD parameterization with the squared control box for the medium grid in combination with Iterative multigrid and the defect correction preconditioner method. For the first case, a drag reduction of about 16.4% was achieved and for the second case a benefit of 19.95% was found.

3.5.3. CAD based parameterization

Figure 10 shows the convergence histories of all considered test cases, using the CAD parameterization (see Table 2). Analogue to the optimization with FFD parameterization, 10 design cycles were executed for each test case. The maximum drag reduction was found with 21.76% by using the finest computational mesh. By using the medium resolved grid, with 30 design variables, a benefit of 17.69% could be achieved. The augmentation of the design variables to 54 effects a further drag reduction of 19.5%. The test case with the defect correction preconditioning for solving of the adjoint solution returns the lowest drag reduction with 8.28% (13.08% with the coarse grid). This is remarkable, as this technique enable a better converged and consequently a more precise solution of the adjoint equation. One assumption is that the optimization algorithm finds with the improved sensitivity a small local minimum. This would also explain why there is nearly no movement in the convergence history beside the tries that return an invalid computational grid.

3.5.4. Optimized geometry

Figure 11 shows the optimized surface for the three considered parameterization methods. Independent from the parameterization, the optimum is found by deforming the round baseline shape into a more edged geometry. Therefore the target surface, upstream from the separation line is pulled inwards while the surface downstream of the separation line is pulled outwards, forming two bumps. This way the beginning of a boat tail is formed, providing a contraction ratio, allowing the attached flow to proceed further downstream, enabling a better re-pressurization (see Figure 12). Consequently the pressure drag of the blunt fuselage is similarly reduced for the three methods (Best result with CAD and finest mesh).

Theoretically the optimum shape would be a complete boat tail, avoiding any flow separations. This optimum could not be found with the used gradient based optimization algorithm. Such geometry would require a large backward deformation of the surface behind the separation line, while the inward deformation in front of the separation should remain relatively small. The problem is that the sensitivity of the design variables is converse. The variables, responsible of the deformation in front of the separation line have a high sensitivity as they directly influences the location of the separation line, while the design variables, responsible of the deformation behind the separation line have a small sensitivity due to the separated flow. This leads to the effect that the optimizer is not able to sufficiently pull back the shape inside the separation area without pulling the shape, in front of the separation line, to far inward, causing an earlier separation. This effect is revealed by the high fluctuation range of the drag function during the optimization with the FFD parameterization method (see Figure 8 and Figure 9). The augmentation of the design variable number (from 30 to 56) shows to have no influence on this behaviour (Figure 8).

The applied CAD parameterization is not able to pull the surface in backward direction (see Chapter 3.3.2), which excluded the formation of a boat tail. In consequence the high fluctuating cost function behaviour could not be observed for these test cases, with exception of the case with the finest computational grid. This can be explained with the increased sensitivity of the separation location by the higher grid resolution.

4. GRC-2 COMMON H/C PLATFORM

4.1. Configuration

During the Clean Sky GRC-2 project, a common H/C platform was defined by the project partners to represent the baseline of a heavy helicopter configuration [10]. The model is based on the GOAHEAD fuselage [18] with additional sponsons (see Figure 13 (left)). One task of the project is to reduce total drag force by optimizing the sponsons shape. Figure 13 (right) shows the baseline sponsons. The red marked area is constrained for inwards deformation to conserve the inner space to host the landing gear. At the beginning of the project, an additional restriction was to prohibit forward deformation of the sponsons nose. This constrain was softened during the project to enable a larger range of possible shapes.

The design point was given for forward flight with $Ma=0.204$ and a fuselage pitch angle of $\alpha = -1.8^\circ$. The reference length was defined as 1m to get a

Reynolds number of about 4.8 million. All relevant data of the design point are summarized in Table 3. Due to the parameterization method, three different sponsons shape are used as start geometry for the optimization. The first version is the given baseline that can be used with the FFD parameterization method. To parameterize the sponson with CATIA-V5, the sponson had to be reconstructed parametrically. Therefore, the second version is slightly different to the base line and possesses a fillet for the sponson-fuselage junction. To further improve the drag reduction, a third version was applied with a swept nose with the objective of reducing the horse shoe vortex of the sponson-fuselage junction. The three considered start solutions are illustrated in Figure 14.

Table 3: Flow condition for common H/C platform sponsons optimization

α [°]	V_∞ [m/s]	Ma [-]	ref. Length [m]	ref. area [m ²]	Re [10 ⁶]
-1.8	70	0.204	1	1	4.8

4.2. Computational grid

To reduce the computational costs during the optimization process, the common H/C fuselage was simplified. Therefore all upper structures were removed i.e. engine cowling, mast fairing and exhausts, as their influence on the sponsons aerodynamic is considered small. Additionally the empennage was removed and replaced by a symmetric cone. The modified fuselage model was covered with a 30 layer thick prism coat with a total high of 24 mm to resolve the boundary layer. The farfield is situated on a sphere with a $12 \times l$ radius ($l = model\ length = 4m$). For the grid resolution, a compromise had to be found between sufficient reliable flow resolution and a manageable number of grid points for the adjoint solver. The result is a grid with 5.5 million grid points, whereby most points are located around the sponsons and in the wake area of the fuselage, as these regions are from special interest for the optimization task (see Figure 15). For the three different test cases, the grid was locally adapted to the actual sponsons shape (see Figure 15).

To validate the results of the optimization, a re-computation of the modified sponson on the complete configuration will be compared with the baseline common H/C platform without rotor head. Therefore an additional computational grid was generated. Figure 16 shows the grid with 6.26 million points. The prism layer and the grid resolution are mainly inherited from the simplified grid. Only the wake area of the afterbody, including the back door surface was refined. To adapt the mesh to the optimized geometry, the possibility of locally grid modification was applied.

4.3. Parametrization

4.3.1. Free Form Deformation

Analog to the ROBIN-mod7 test case, a rectangular and a shape adapted deformation box was tested, using a surrogate grid for the surface deformation. The rectangular box has the dimension $i=4$, $j=10$ and $k=4$. All control points, laying on the symmetry plane nearest face were fixed so that a total number of 124 design variables are remaining (see Figure 17 (left)).

To apply a shape adapted control box around the sponson, it is necessary to use 3 individual boxes to avoid strongly deformed cells (see Figure 17 (right)). At this place the sponson was split in a front, middle and a trailing edge part. The front box has the dimension $i=5$, $j=5$, $k=2$, the middle part $i=13$, $j=14$, $k=2$ and the trailing edge box $i=5$, $j=5$, $k=2$. Here again only the control points on the outer faces are considered as design variable with the displacement direction normal to the target surface. At the conjunction of the boxes, the common control points of both boxes are considered as one design variable. This combination leads to a total number of 206 design variables.

In both cases the constraints (see Figure 13 (right)) were fulfilled by limiting the resulting displacement vectors for the grid adaption by RBF-deformation. Therefore all inward pointing displacement vectors, located on the red marked surface are set to zero. Additionally it was possible, to reduce the vector length in the front part to avoid a deformation beyond the sponsons nose.

4.3.2. CAD based parameterization

For the CAD based parameterization, the sponson was reconstructed by using a longitudinal and six

lateral profiles (see Figure 18). The profiles shapes are defined by B-splines whose control points location are used as design variables. The moving directions of the control points are illustrated in Figure 18 (bottom). The constrained area was retained from the baseline configuration as no significant outward deformation was expected at this location. An additional design variable was given to define the radius of a fillet to ease the sponson-fuselage junction. It turned out, that the fillet function tends to instabilities depending on the sponson-fuselage intersecting line. To keep this function for the optimization, several control points of the lateral profiles, which cause an unfavourable intersecting line, had to be fixed. This leads to a total number of 68 design variables.

After changing the constrains in order to allow forward deformations of the sponsons, a swept nose was added to the model as this kind of device showed to reduce drag during pre-investigations. The parameterization of this swept nose is shown in Figure 19. Eight additional design variables define the shape by two B-splines, a sweep angle and a pitch angle.

4.4. Test Matrix

In Table 4 all considered test cases for the sponsons optimization are summarized. Beside the different parameterization methods, the benefit of ignoring the no forward deformation constrain was investigated by adding a swept nose in the CAD-based optimization and by allowing forward deformation for the FFD test case with a square control box.

Table 4: common H/C platform sponsons optimization test matrix

Name	Parameterization methode	design variables	Forward deformation constrain	ΔC_d
CP_FFD_ad_206	FFD with shape adapted control box	206	respect	2.3%
CP_FFD_sq_124	FFD with square control box	124	respect	1.61%
CP_CAD_nN_68	CATIA V5 (CAD) without swept nose	68	respect	2.01%
CP_CAD_wN_76	CATIA V5 (CAD) with swept nose	76	ignore	2.42%

4.5. Results

4.5.1. Baseline

Due to the necessity of reconstructing the sponsons shape by a parametrical CAD model, the start geometry for the CAD-based optimization deviates from the baseline shape that is used for the FFD based parameterization. Therefore three individual start solutions had to be computed. The configuration with the original sponsons returns a drag coefficient of 0.0401 and the re-constructed sponsons a C_d -value of 0.0393. The solution with the swept nose is predicted with a drag coefficient of

0.0387. At this place it can be observed that the re-constructed sponson with the swept nose already has a beneficial influence on drag compared to the original shape.

Figure 20 shows the flow conditions on the sponsons and the back door ramp of the simplified common H/C platform fuselage. The flow is characterized by the horse shoe vortices of the sponsons and the flow separation on the back door surface. For the case with the additional swept nose the horse shoe vortex is significant reduced on the down side of the sponson, compared to the original

sponsons. This change further effects the formation of the separation area on the backdoor.

The investigation of the influence of the perturbation step size on the resulting gradient shows good consistent results with 0.1mm and 0.01mm for the FFD test case. Therefore the step size of 0.1mm was chosen for the optimization. For the CAD test cases, the step sizes of 1mm and 0.1mm returns sufficient consistent gradients. This leads to the selection of a 0.1mm perturbation step size

4.5.2. Free Form Deformation

Each case, considered in Table 4, was executed with 20 design cycles. Figure 21 shows the history of the drag difference during the optimization with the two different FFD parameterization methods (shape adapted control box and squared control box). To enable a meaningful comparison of the following values, the achieved benefits are all referred to the total drag coefficient of the complete baseline configuration. In both cases several tries returns an invalid computational grid, especially to the end of the optimization. This indicates that the grid deformation is a limiting factor. Nevertheless it was possible to achieve a drag reduction of 2.3% referred to the total drag of the complete baseline configuration by using the shape adapted control boxes. Figure 22 (left) shows the modified shape. The nose of the sponson is pulled upwards and got a more tapered shape. On the lower side of the rear part, the geometry is pulled inwards and forms a kind of rear loading section similar to wing profiles. The trailing edge is deformed to a bump.

The parameterization with the squared control box returns a lower drag benefit of 1.61% referred to the total drag of the complete baseline configuration. By having a look on the resulting surface (see Figure 22 (right)) it can be again observed that the nose is pulled slightly upwards while the shape is tapered. At this place the optimizer tries to additionally pull the nose forward which is stopped by the applied constrains.

4.5.3. CAD based parameterization

Both approaches with CAD-based parameterization were optimized during 20 design cycles. The history of the cost function for the two optimizations is illustrated in Figure 23. Here again, the change in drag is referred to the complete baseline configuration. For the test case without swept nose it can be seen that already the remodelled CAD shape returns a drag reduction of about 1%. During the optimization, the drag could be further reduced by a second percent, which leads to an optimization of 2.01%. Compared to the previously observed optimizations, this optimum is already found after the second design cycle. The following tries leads several times to either an invalid CATIA model or a

destructured computational grid.

By having a look on the resulting surface in Figure 24 (left), a particular nose shape revealed. Similar to the previous optimization with the FFD parameterization, the nose is tapered. But in this case the leading edge remains blunt, without hitting the forward deformation constrain. This leads again to the assumption that a local minimum is found, where the optimizer, additionally limited by the CAD-model stability and the grid deformation, is not able to escape. The rear part of the sponson is again pulled inward at the lower side, as observed before. The fact the displacement remains smaller than for the FFD optimization is due to the fact that the remodelled shape already deviates in this direction, compared with the original baseline.

The addition of a swept nose on the remodelled sponson reduces the drag of about 1%. Therefore the optimization was started with a shape that already has a benefit of about 2% referred to the complete baseline configuration. During the optimization it was only feasible to reduce the drag by about an additional half percent. Here again, the minimum was found after few design cycles. Already the third design cycle returns a benefit of 2.42% that could not be improved by further design cycles. Compared to the approach without swept nose, the optimization runs stable with only one try that returns an invalid computational grid.

Figure 24 (right) displays the shape changes for the optimum shape. Here again the nose got tapered and the swept nose was pulled slightly upwards. Contrary to the deformation by the FFD parameterizations, the leading edge of the nose is pulled downwards. The rear part of the sponsons was modified analogue to the previous observed optimizations.

4.5.4. Optimized geometry

The breakdown of the achieved benefits on the different parts of the fuselage is illustrated in Figure 25 (definition of break down surfaces is illustrated in Figure 13). The results of all four optimizations are compared to each other. Here again all obtained benefits are set in reference to the complete baseline configuration. It can be seen that the drag reduction is mainly achieved on the backdoor area, the sponsons and the tail, while a drag increase is caused on the rear fuselage. For the case with an additional swept nose, the drag on the middle fuselage is also significantly increased. This is due to the fact that the surface mesh of the middle fuselage was projected on the swept nose to keep the grid topology as similar as possible compared to the baseline grid. This way the swept nose was considered for the drag breakdown as part of the middle fuselage, instead of the sponsons.

To verify the validity of the optimizations, the respectively best shapes of both parameterization methods were recomputed on the complete configuration. The resulting benefit breakdown is additionally included in Figure 25. Compared to the results of the simplified model, the predicted drag reduction is predicted lower. The complete configuration with the optimum shape of the FFD parameterization returns a higher drag reduction on the backdoor. This additional benefit is compensated by drag rises on nearly all remaining parts with exception of the fuselage front, the mast fairing and the shaft-cowling, as the sponsons modification had no influences on these parts.

For the solution with swept nose, the benefit on the backdoor, the sponsons, the rear fuselage and the tail deviates from the predicted drag changes by the optimization results. The differences on the tail could be explained by the different geometry of the simplified model. However the significant differences on the sponsons for both re-computations indicate that the benefits during the optimization are also caused by the deformed computational grid.

Figure 26 illustrates the flow solution on the surface of complete baseline configuration and the two considered re-computations of the optimized sponsons. Compared to the baseline of the simplified model (see Figure 20), the flow displacement caused by the engine cowling and the exhausts additionally influences the flow conditions on the backdoor, which causes a different characteristic of the separation.

Comparing the results of the two optimized geometries it can be seen that mainly two different mechanisms are responsible for the drag reduction. The first one is to redirect the sponsons wake to suppress the flow separation as it could be observed for the optimum of the FFD parameterization. This causes a better re-pressurization of the flow on the back door ramp. The second mechanism is to taper the nose. This way the stagnation area on the leading edge is reduced and the horse show vortex is weakened. This effect could be additionally amplified by applying a swept nose in the sponsons-fuselage junction. The tapering of the sponsons front also causes a reduction of the suction peak on the down side so that the down wash and the depending induced drag force are reduced.

5. CONCLUSIONS

A CAD-based and a Free Form deformation based parameterization method were integrated into a gradient based optimization chain. The capabilities of this optimization tool are demonstrated for two different examples. The first example consists of the drag optimization of the blunt afterbody of the ROBIN-mod7 fuselage. This relatively simple

geometry was chosen to investigate the impact of computational grid resolution, number of design variables and the applied solving method for the adjoint equation on the optimization process.

The considered parameterization methods return all similar optimized results with a maximum drag reduction of 21.76%. Nevertheless this example reveals the weakness of the optimization algorithm to find the global optimum for a complex solution area with a high range of sensitivities for the design variables.

The second example is the optimization task of the common H/C platform from the Clean Sky GRC2-project. For the optimization the fuselage had to be simplified to enable the flow evaluations in a reasonable time and to insure a solution of the adjoint problem. For the CAD-based parameterization method, an additional swept nose was applied on the sponsons front.

The FFD parameterization shows the highest drag reduction compared to its start solution. Referred to the complete baseline configuration a drag reduction of 2.3% could be achieved. At this place it turns out that the computational grid adaption by RBF-deformation fails several times for larger deformations in the intersection of the sponsons with the fuselage.

Due to the remodelling of the Sponsons shape in CATIA V5, the CAD-based optimization starts with a slightly different geometry which already shows an improvement of the resulting drag. This benefit was additionally increased by the application of a swept nose. Starting from this solution, the optimization chain was only able to find small further improvements, which leads to an optimum of 2.42% drag reduction, compared to the complete baseline configuration.

To verify the fidelity of the optimization of the simplified model, the optimal shapes of the different parameterization methods are re-computed on the complete fuselage configuration. This verification shows in both cases that the drag benefit is reduced to about 1.5% in both cases. One reason is the drag rise on parts that had not been considered in the simplified model. Another reason is the different drag prediction directly on the sponsons. This fact reveals that the benefit, found by the optimizer is not only caused by the shape but also by the deformation of the computational grid. This effect could be avoided by regenerating the computational grid during the design steps by the costs of higher computational effort and higher cost function noise due to differences in the unstructured grid topology.

The considered examples show that both parameterization methods are able to return similar optimization results. The benefit of the FFD method

is the fast and easy parameterization of relatively simple geometries. The CAD-based parameterization is much more time consuming and requires advanced skills for CATIA V5. These drawbacks are compensated by the ability to parameterize complex geometries and enabling a more flexible investigation of different details like position, orientation and scaling of different parts relatively to each other for example. Consequently the right choice of the parameterization method is mainly depending on the given task.

ACKNOWLEDGMENTS

The Author would like to thank the colleges of the DLR Institute for Aerodynamics and Flow Technology for their productive hints and comments that helped to realise this work. Additional thanks go to the European Community's Seventh Framework Programme (FP7/2007-2013) for the Clean Sky Joint Technology Initiative under grant agreement n^o CSJU-GAM-GRC-2008-001 for providing the funding of these researches.

REFERENCES

- [1] Jameson, A., Martinelli, L., "Aerodynamic Shape Optimisation Techniques Based on Control Theory", CIME (International Mathematical Summer Center), Martina Franca, Italy, 1999
- [2] Dwight, R.P., "Efficiency Improvements of RANS-Based Analysis and Optimization using Implicit and Adjoint Methods on Unstructured Grids", Ph.D. thesis, University of Manchester, Manchester, UK, 2006
- [3] Brazillon, J., Dwight, R. P., "Aerodynamic Shape Optimisation using the Discrete Adjoint of the Navier-Stokes Equations: Applications towards Complex 3D Configurations", Proceeding of the CEAS/KATnet II Conference on Key Aerodynamic Technologies, Paper No. 36-1, May 2009
- [4] Segerberg, T. W., Parry, S. R., "Freeform Deformation of Solid Geometric Models", Proceedings of SIGGRAPH 1986, Dallas, USA, Aug. 18-22, 1986
- [5] Q.Zhang, J.-H. Wendisch, J.-D.Lee, "An Adjoint-Based Optimisation Method for Helicopter Fuselage Backdoor Geometry", 36th European Rotorcraft Forum 2010, 7.-9. Sep. 2010, Paris, France
- [6] Wentrup, M., Khier, W., Zhang, Q., "Drag reduction of a transport helicopter by application of an adjoint-based fuselage optimization chain and modification of the rotor head", Greener Aviation conference, Brussels, Belgium, 2014
- [7] Zhang, Q., Garavello, A., D'Alascio, A., Schimke, D., "Advanced CFD-based Optimization Methods Applied to the Industrial Design Process of Airframe Components at Airbus Helicopters", American Helicopter Society 70th Annual Forum, Montréal, Canada, 2014
- [8] Dassault Systèmes CATIA V5 <http://www.3ds.com/products-services/catia/> [27.05.2015]
- [9] Schaeffler, N., Allan, B., Lienard, C., Le Pape, A., "Progress Towards Fuselage Drag Reduction via Active Flow Control: A Combined CFD and Experimental Effort". 36th European Rotorcraft Forum, 2010
- [10] D'Alascio, A., Kneitsch, T., "Specification of Geometrical Constraints and of the Design Points for Common Helicopter Platform Optimization Subtasks", CSJU/ITD GRC/RP/2.2.2/32024, 2011
- [11] Fletcher, R., Reeves, C. M., "Function Minimization by Conjugate Gradient", Computer Journal., 7, 149-154, 1964
- [12] Gerold, T., Friedrich, O., Evan, J., Galle, M., "Calculation of Complex Three-Dimensional Configurations Employing the DLR-TAU-Code", AIAA paper 167, 1997
- [13] Spalart, P., Allmaras, S., "A One-Equation Turbulence Model for Aerodynamic Flows", AIAA Paper 92-0439, 1992
- [14] Saad Y., Schultz, M.H., "GMRES: A Generalized Minimal Residual Algorithm for Solving Nonsymmetric Linear Systems", SIAM J. Sci. Stat. Comput., 7:856-869, 1986
- [15] Allen, B.; Schaeffler, N.; "Numerical Investigation of Rotorcraft Fuselage Drag Reduction using Active Flow Control", American Helicopter Society 67th Annual Forum, Virginia Beach USA, 2011
- [16] Martin, P., Overmeyer, A.; Tanner, P., Wilson, J.; "Helicopter Fuselage Active Flow Control in the Presence of a Rotor", American Helicopter Society 70th Annual Forum, Montréal, Canada, 2014

- [17] *POINTWISE USER MANUAL*. Forth Worth, Texas, USA , s.n., 2012.
- [18] Palke, K. "The GOAHEAD Project" 33rd European Rotorcraft Forum, Kazan, Russia, 2007

APPENDIX

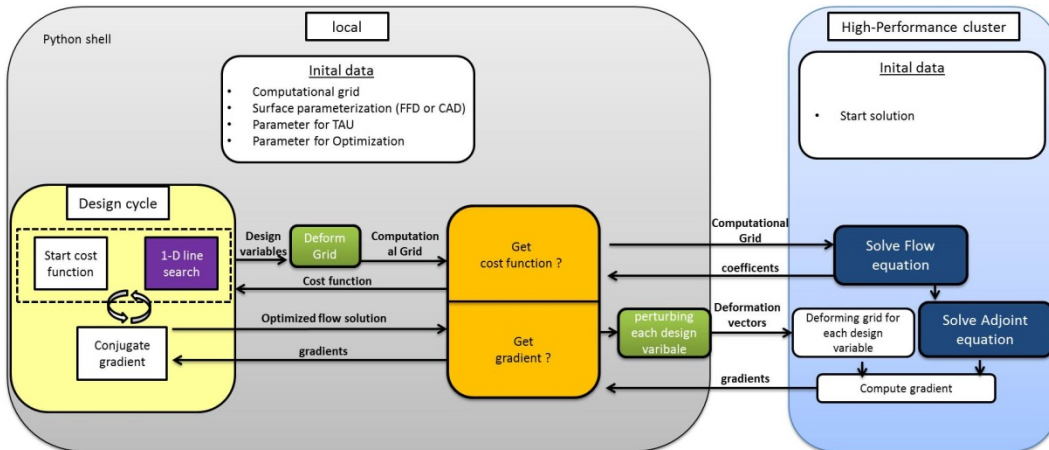


Figure 1: Optimization Chain

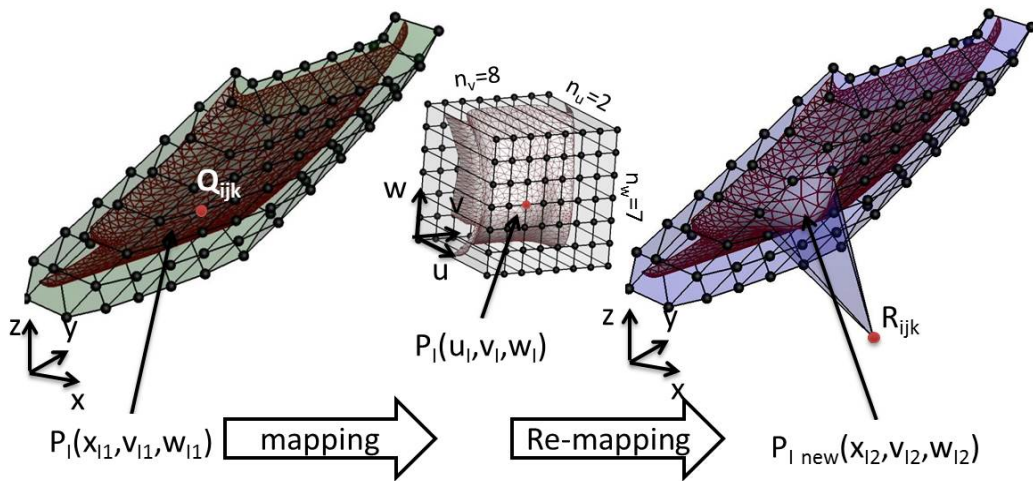


Figure 2: Principle steps of FFD

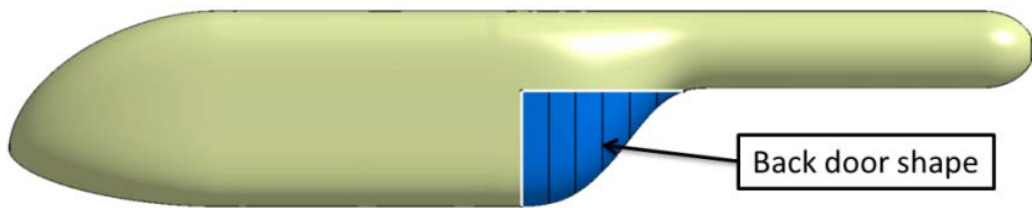


Figure 3: Robin mod-7 fuselage

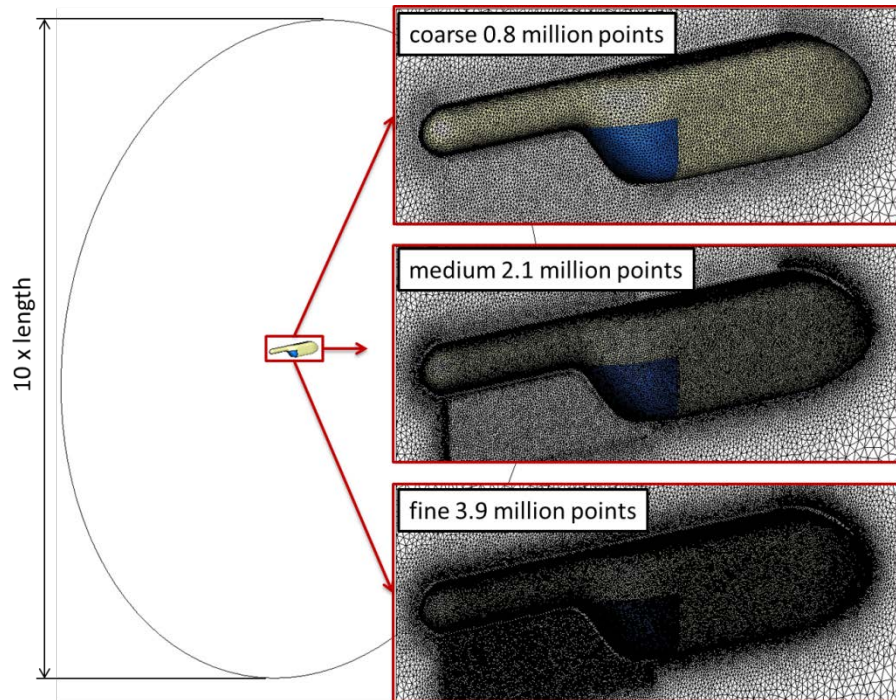


Figure 4: computational grid for ROBIN-mod7 optimization task (top: coarse grid; middle: medium grid; bottom: fine grid)

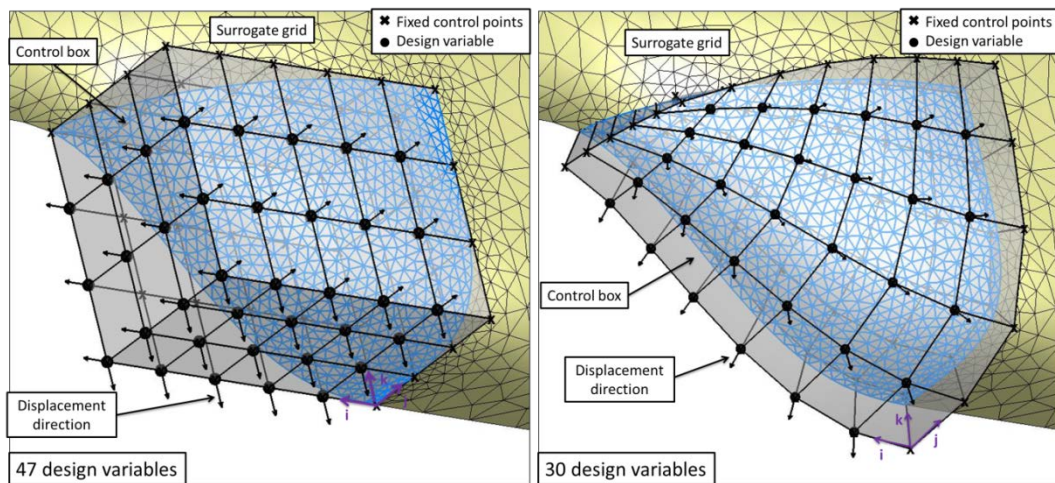


Figure 5: FFD parameterization of the ROBIN-mod7 back door with orthogonal box (left) and shape adapted box (right)

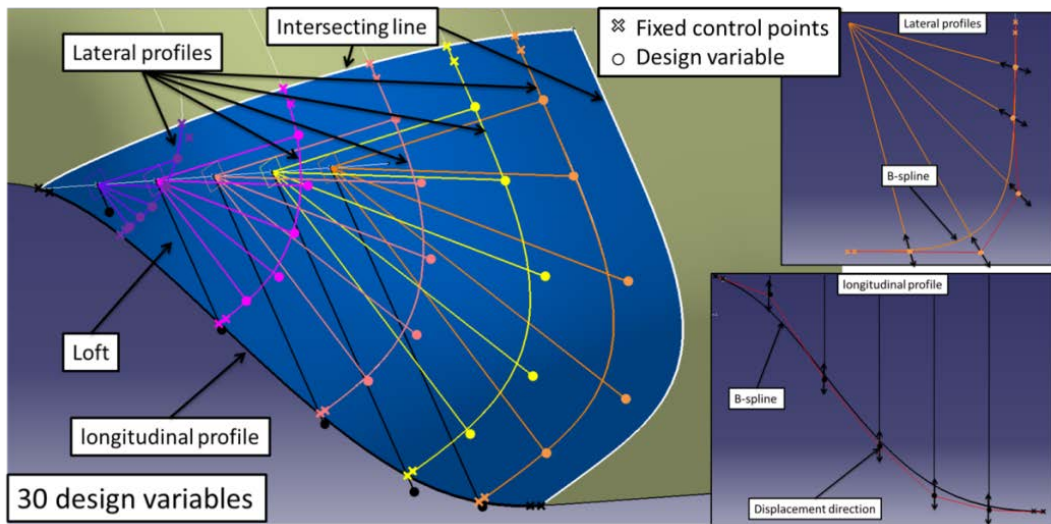


Figure 6: CATIA V5 parameterization of ROBIN-mod7 back door

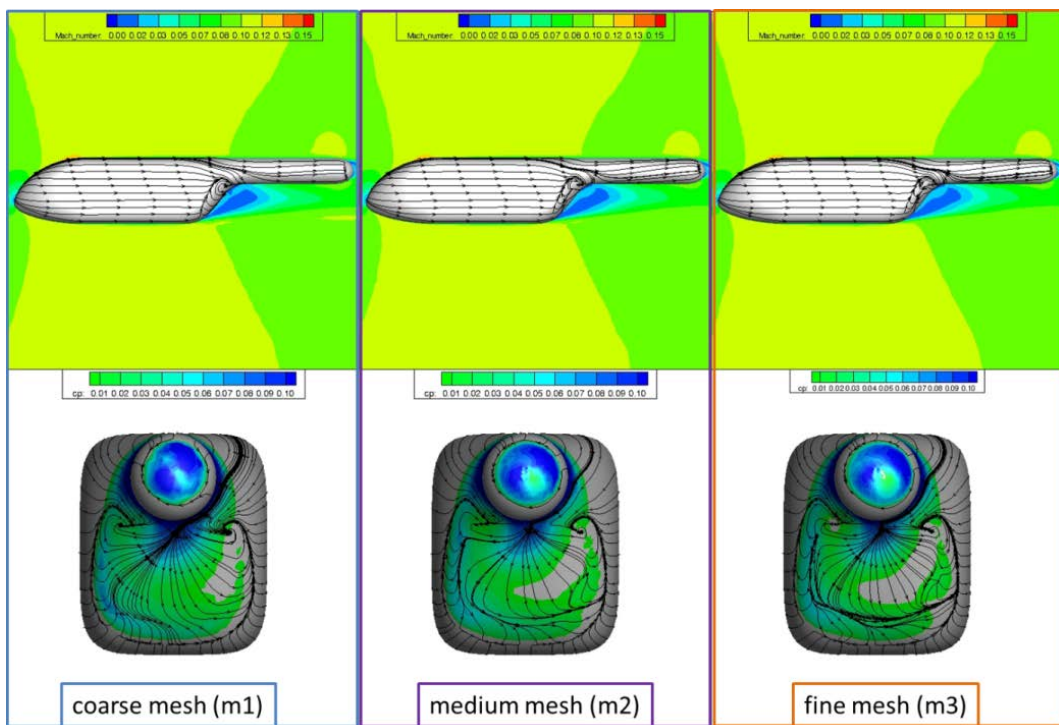


Figure 7: Flow solution of coarse (left), medium (middle) and fine (right) computational mesh

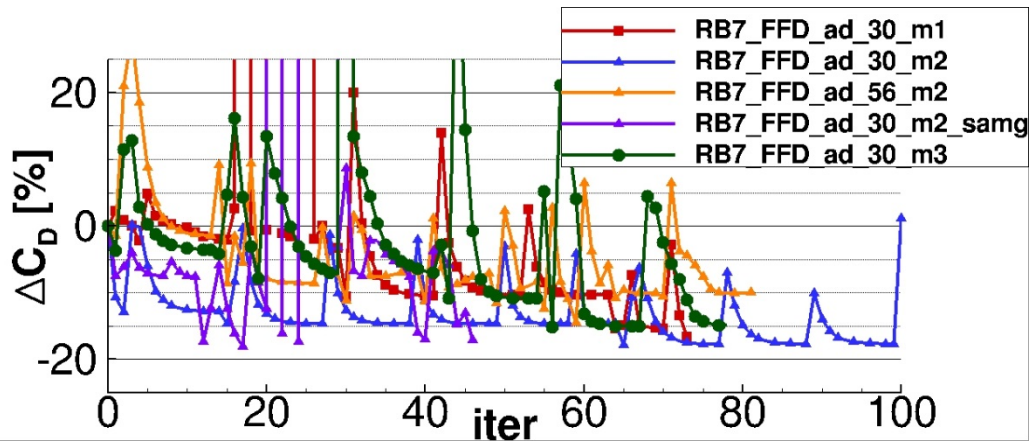


Figure 8: Convergence history of optimization using the FFD parameterization technique with shape adapted control box for all three grid and different numbers of design variables (30 and 56)

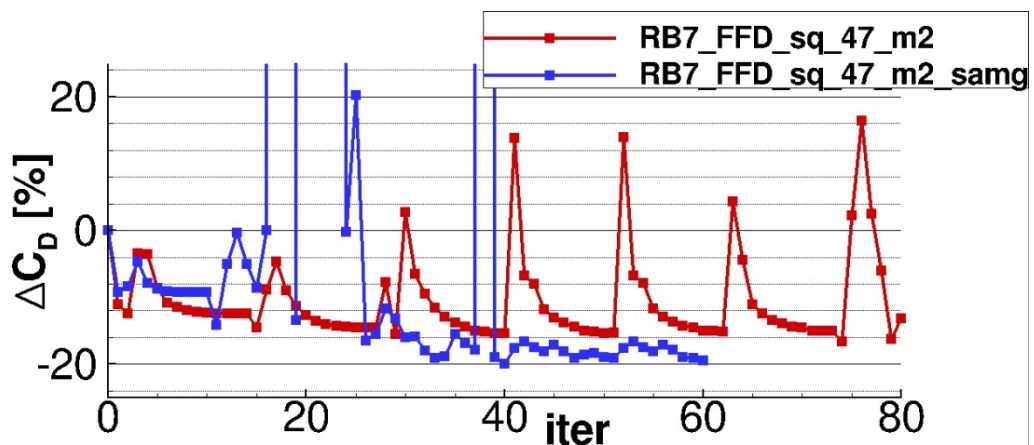


Figure 9: Convergence history of optimization using the FFD parameterization technique with shape squered control box for the medium resolved grid with iterativ multigrid preconditioning and defect correction preconditioning

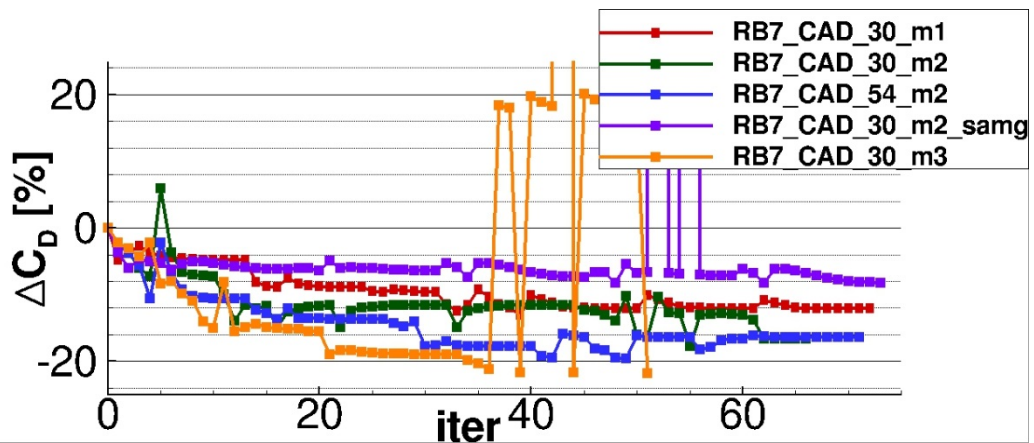


Figure 10: Convergence history of optimization using the CAD parameterization technique for all three grids and and different numbers of design variables (30 and 54)

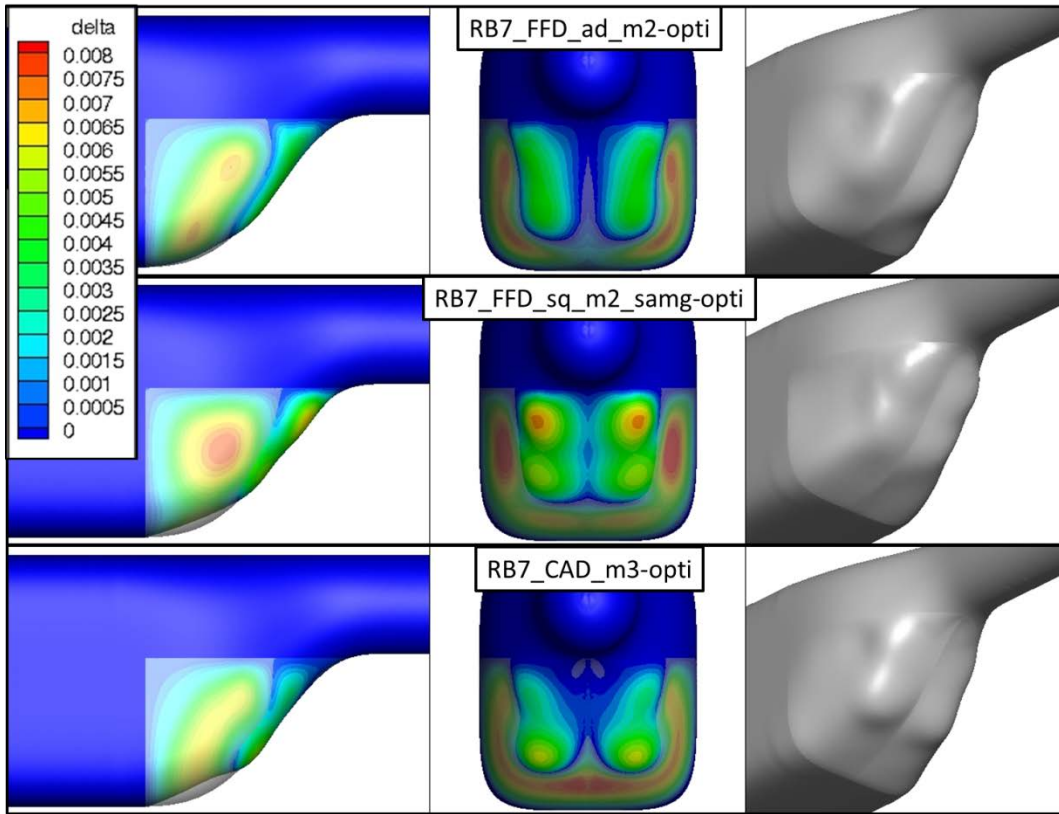


Figure 11: Optimized shapes: RB7_FFD_ad_m2 (top), RB7_FFD_sq_m2_samg (middle), RB7_CAD_m3 (bottom)

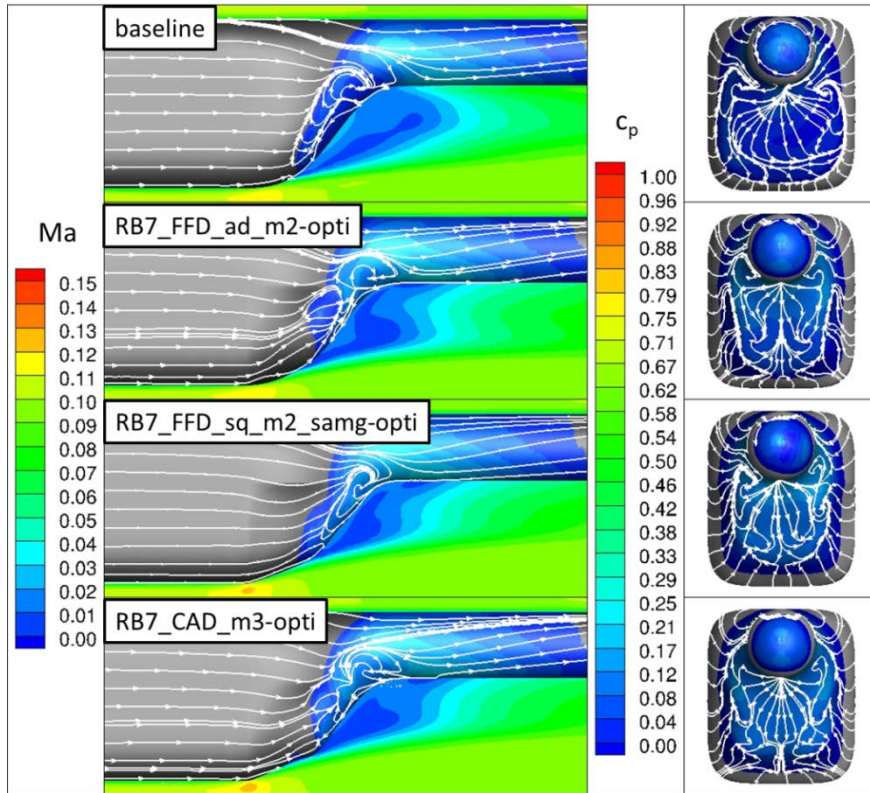


Figure 12: Flow solutions for optimized shapes (Ma cut at $y=0$ and $c_p > 0$ on surface): Baseline (top), RB7_FFD_ad_m2 (top-middle), RB7_FFD_sq_m2_samg (bottom-middle), RB7_CAD_m3 (bottom)

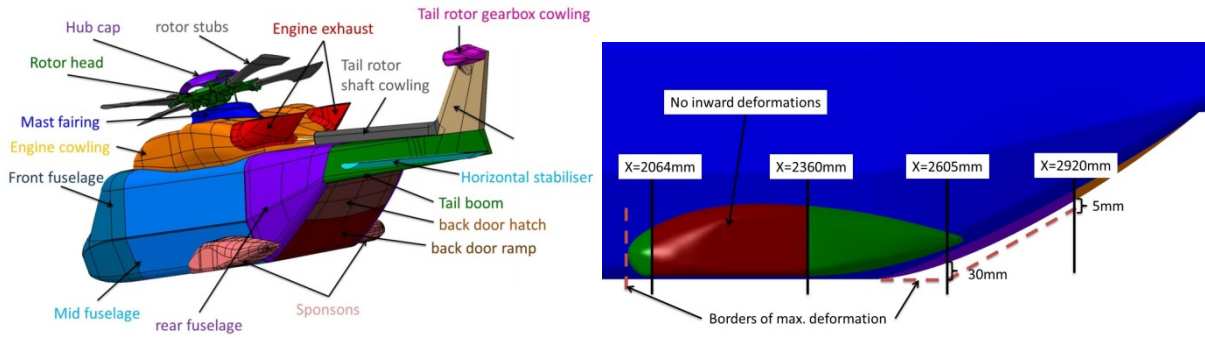


Figure 13: Common H/C platform (left) and geometrical constraints for deformation (right)

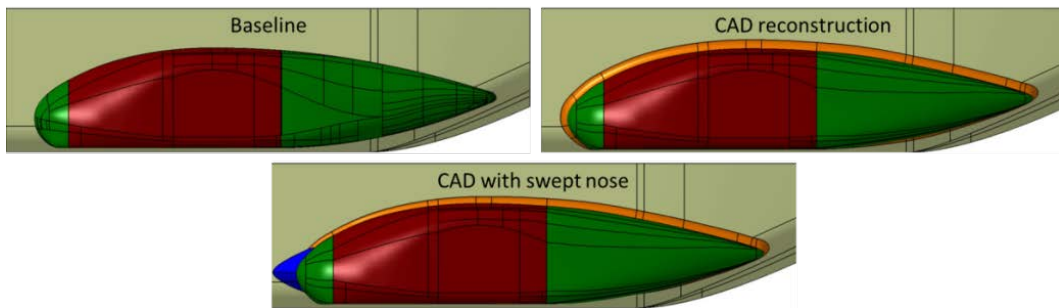


Figure 14: FFD start geometry (left); CAD- start geometry (right); CAD start geometry with swept nose (middle)

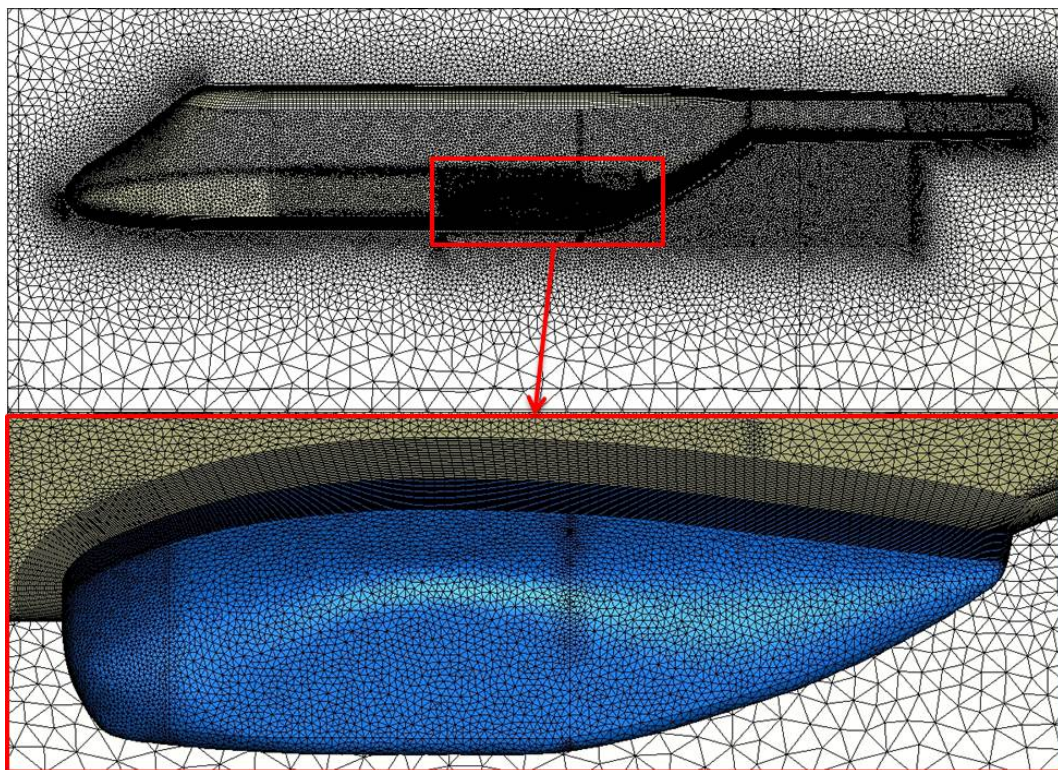


Figure 15: simplified computational grid for common H/C platform sponsons optimization (top: baseline; bottom left: CAD reconstruction; bottom right: CAD with swept nose)

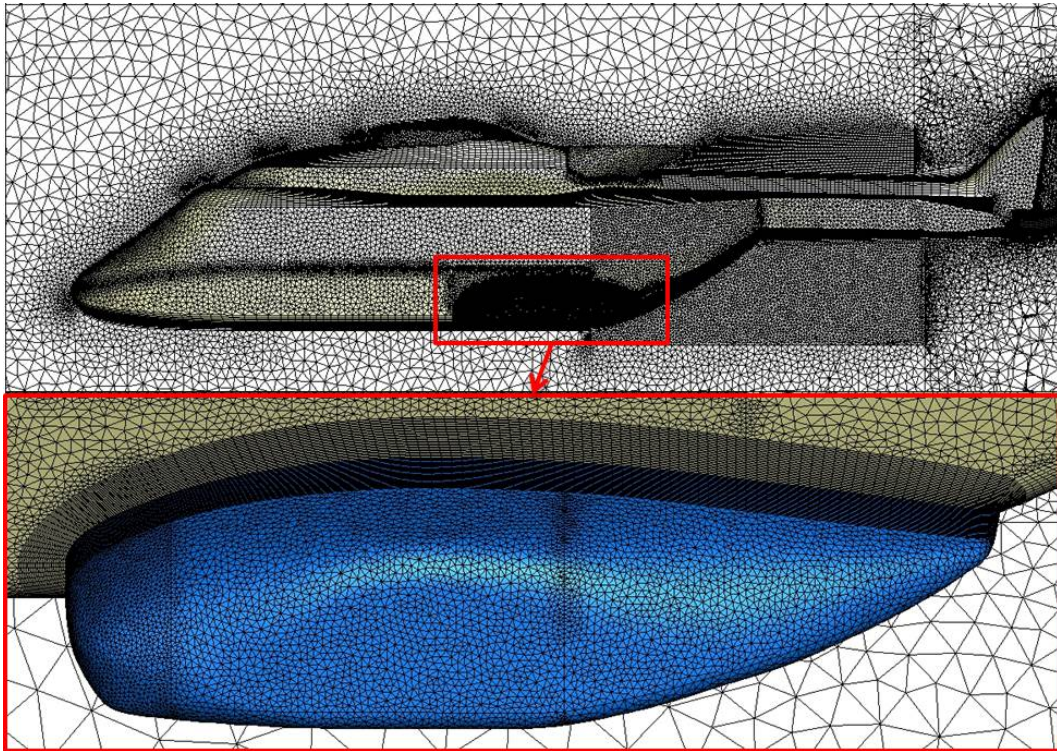


Figure 16: Computational grid of the complete common H/C platform configuration

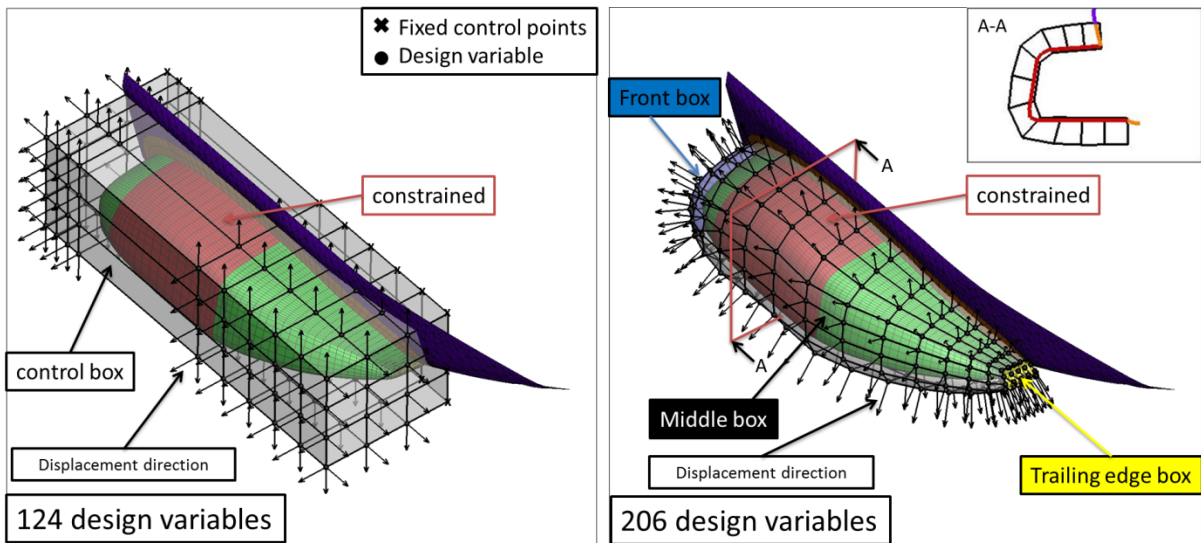


Figure 17: FFD parameterization of the common H/C platform sponson with orthogonal box (left) and shape adapted box (right)

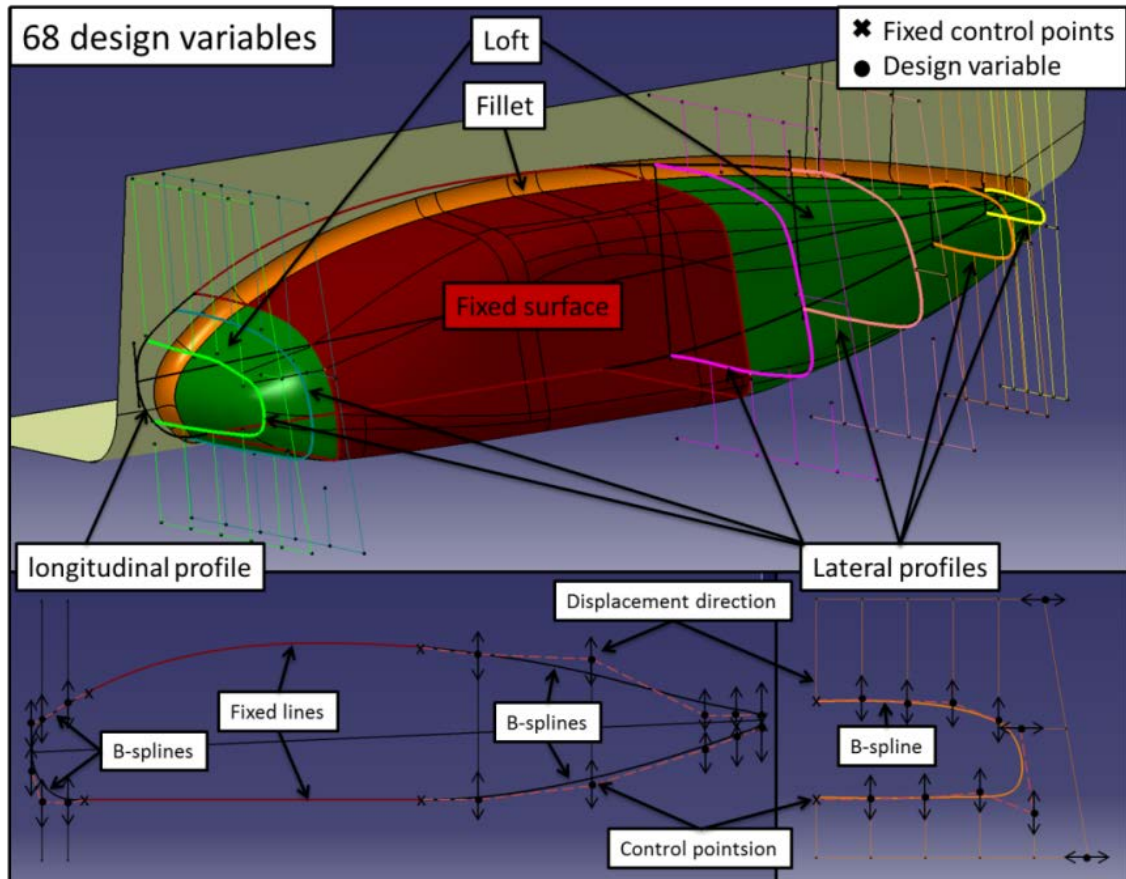


Figure 18: CATIA V5 parameterization of the common H/C platform sponson

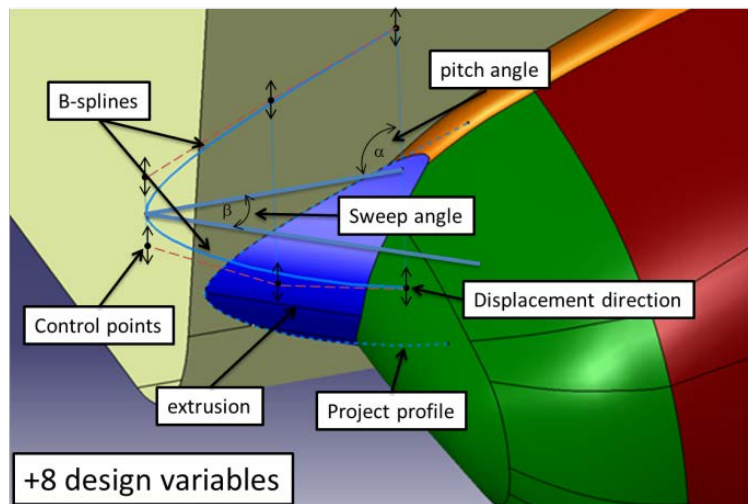


Figure 19: CATIA V5 parameterization of the common H/C platform sponsons swept nose

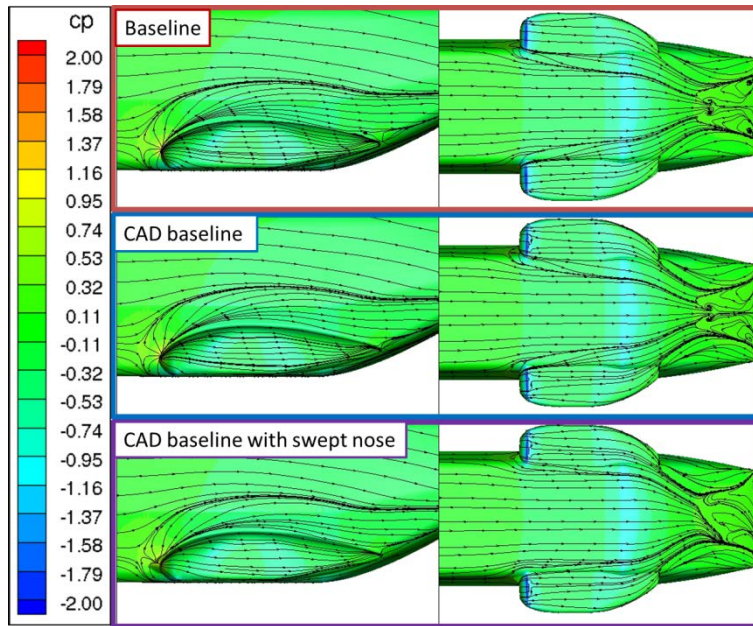


Figure 20: Flow solution baseline (top), CAD remodelled baseline (middle), CAD remodelled baseline with swept nose (bottom)

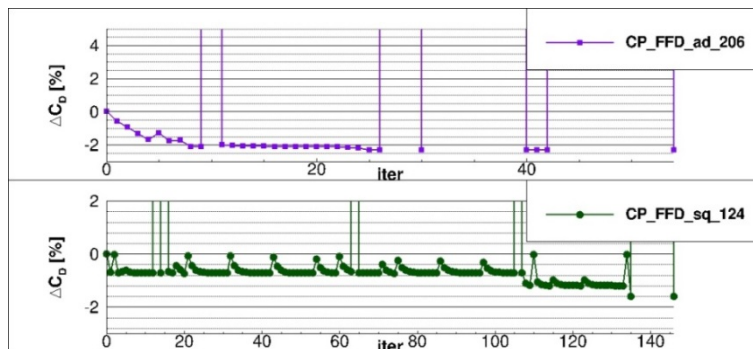


Figure 21: Convergence history of optimization using the FFD parameterization technique with shape adapted control box (top) and with the squared control box (bottom)

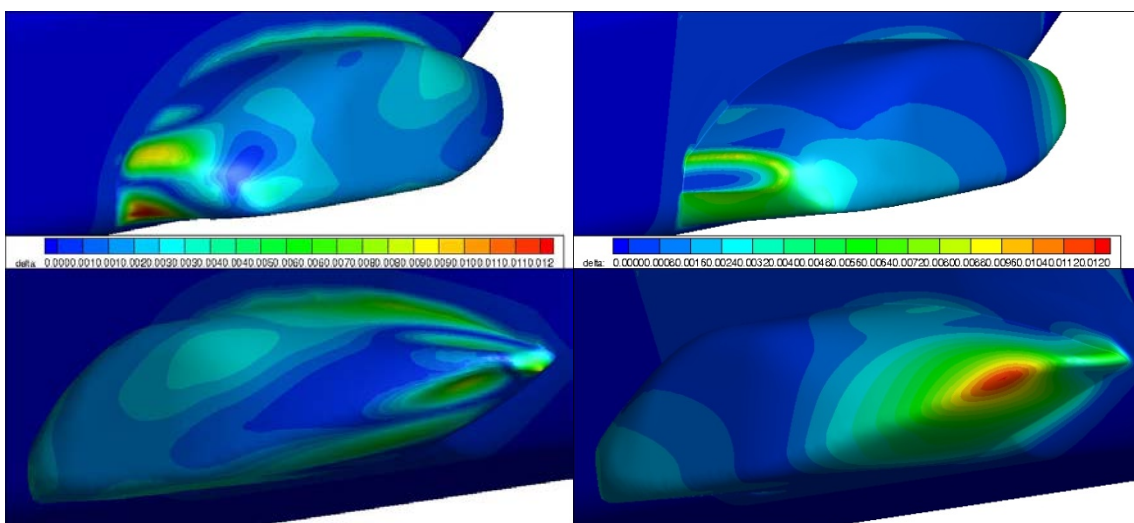


Figure 22: Optimized sponson shape by FFD with shape adapted control box (left) and Optimized sponson shape by FFD with squared control box (right)

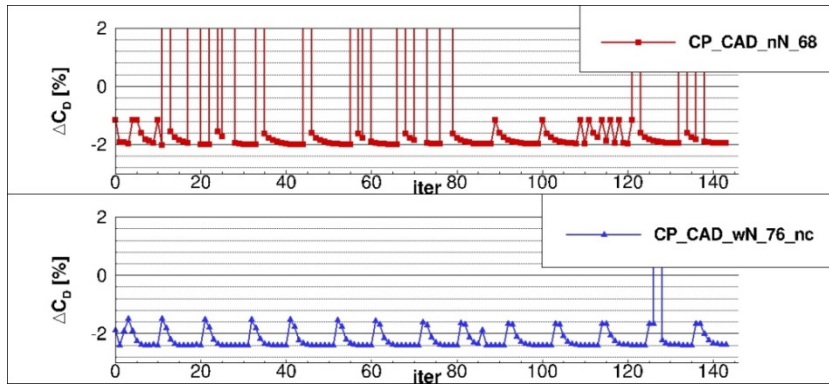


Figure 23: Convergence history of optimization using the CAD parameterization technique (top) and with the additional swept nose (bottom)

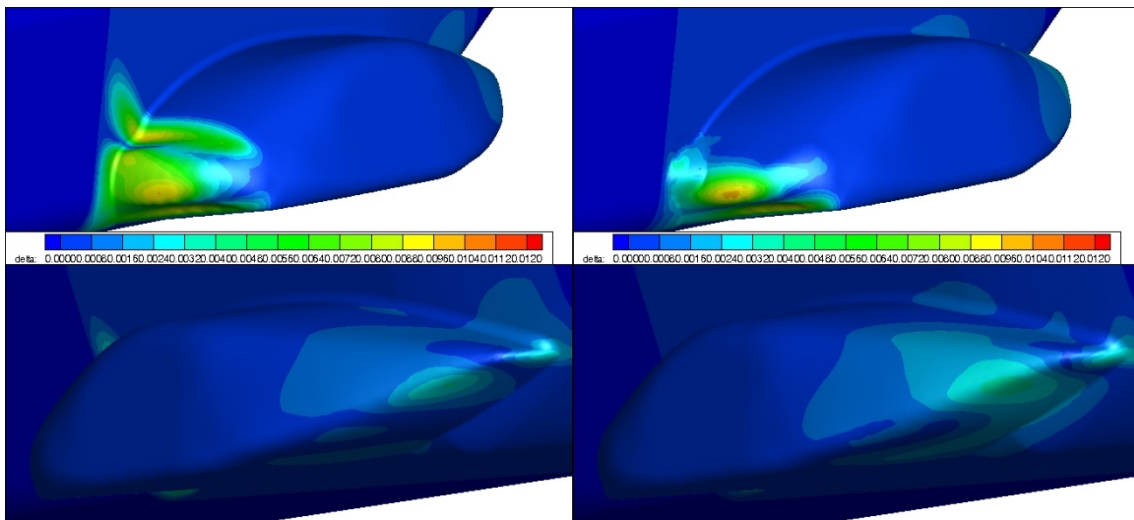


Figure 24: : Optimized sponson shape by CAD parametrization (left) and Optimized sponson shape by CAD parametrization with swept nose (right)

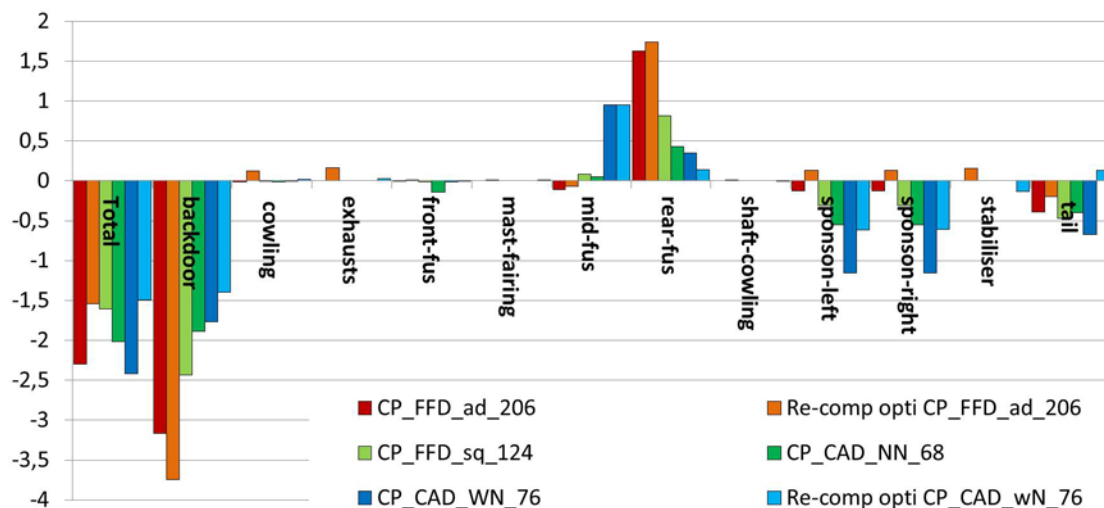


Figure 25: Drag reduction breakdown for all sponsons optimization and the re-computed optimum for the complete configuration

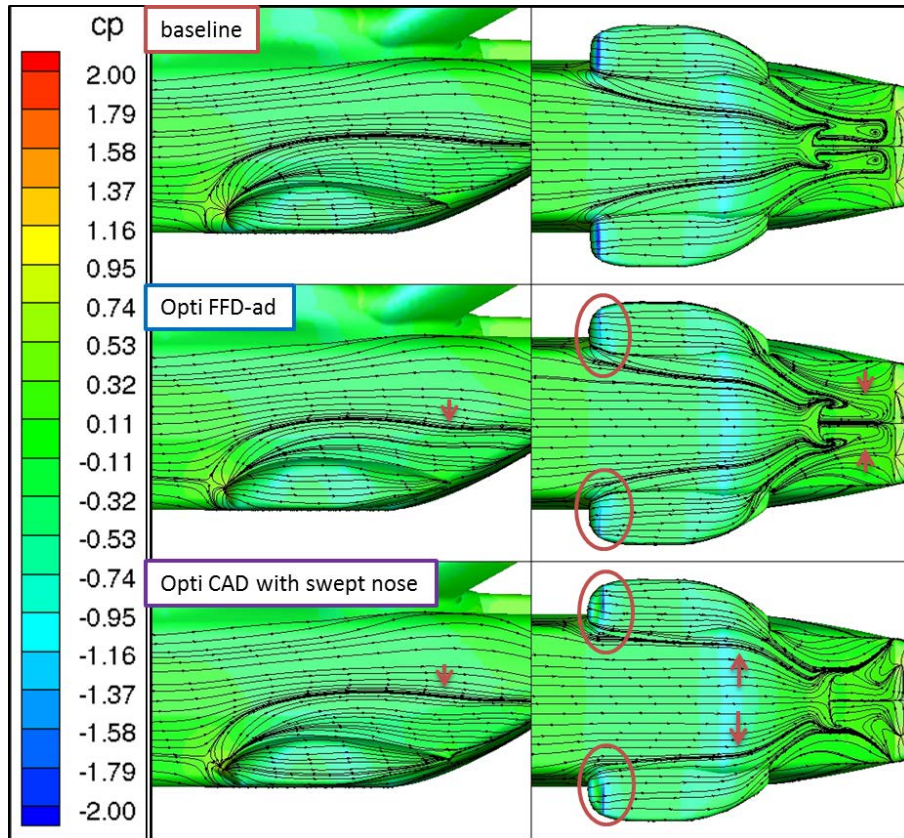


Figure 26: Flow solution of the complete baseline configuration (top), the re-computed optimum with FFD parameterization (middle) and re-computed optimum with CAD parameterization and swept nose (bottom)